Bulletin of the Mineral Research and Exploration

http://bulletin.mta.gov.tr

(U-Th)/He geochronology of supergene iron ores from Attepe, Eastern Taurides, Türkiye: Evidence for Early Pleistocene aridification

Serdar KESKİN*[a] and Taner ÜNLÜ[b]

[a]*General Directorate of Mineral Research and Exploration, Eastern Black Sea District Office, Trabzon, Türkiye*
[b]*Ankara University, Department of Geology, Ankara, Türkiye*

Research Article

Keywords:
Attepe, U-Th/He, Uplift, Iron Deposit, Aridification.

ABSTRACT

The Taurus Mountains form the southern boundary of the Central Anatolian Plateau in Türkiye and represent part of the broader Himalayan-Tibetan orogenic system. Today, they act as a climatic divide, separating the dry, semi-arid interior in the north from the more temperate Mediterranean climate in the south. However, their formation history and climatic impacts remain unclear. In this study, we apply multiple aliquot (U-Th)/He dating to supergene iron-oxide phases from the Attepe iron deposits in the Eastern Taurides to investigate Cenozoic climatic conditions. The ages obtained from four deposits range from ~5.2 to 0.95 Ma, indicating sustained hot and humid conditions conductive to supergene mineralization during the Plio-Pleistocene. The observed decrease in age with depth, reflect a progressive deepening of the weathering front at rates of 6.4 to 18 meters per million years between 5 and 1 Ma. The preservation of supergene iron minerals formed during a stable, warm, and humid period between the late Miocene and Middle Pliocene means the absence of rapid uplift or erosion within the past million years. Instead, the youngest goethite around 0.95 Ma supports the hypothesis that regional climate change, rather than tectonic uplift, was the primary factor of increasing aridity around ~1 Ma.

Received Date: 23.03.2025
Accepted Date: 08.10.2025

1. Introduction

The uplift of high elevation regions such as the Tibetan Plateau and Altiplano-Puna has driven changes in both regional and global climate (Molnar et al., 1993; Allmendinger et al., 1997; Molnar, 2005; Ehlers and Poulsen, 2009). The Central Anatolian plateau (CAP) is the westernmost expression of the Himalayan-Tibetan orogen to the east (Hatzfeld and Molnar, 2010) and covers approximately 120,000 km^2 at an average elevation of around 1 km above sea level (Çiner et al., 2015). It is surrounded by the Pontides to the north, and by the Taurides to the south (Figure 1). The Taurides have an average elevation of 2.4 km and act as an orographic barrier to precipitation. They separate the semi-arid CAP (Schemmel et al., 2013) from the mild Mediterranean climate to the south (Şensoy, 2004). The paucity of terrestrial climate records makes it difficult to accurately determine when the current semi-arid climate became established across the southern margin of the Central Anatolian Plateau (smCAP), and how it relates to the uplift of the Tauride mountains. Consequently, the timing of uplift

Citation Info: Keskin, S. and Ünlü, T. 2025. (U-Th)/He geochronology of supergene iron ores from Attepe, Eastern Taurides, Türkiye: Evidence for early Pleistocene aridification. Bulletin of the Mineral Research and Exploration 178, 33-52. https://doi.org/10.19111/bulletinofmre.1804818

**Corresponding author: Serdar Keskin, serdarkeskin34@gmail.com*

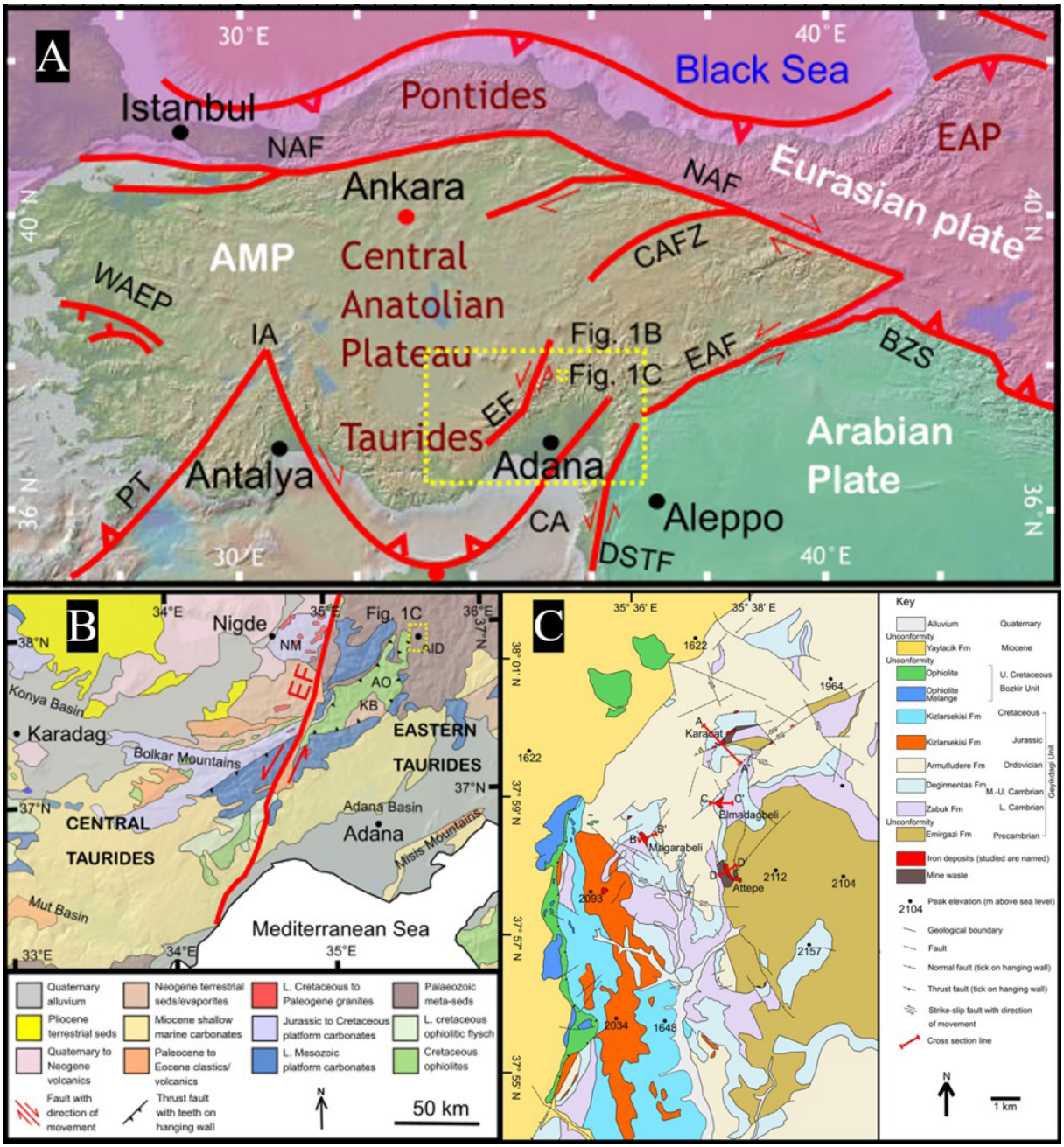

Figure 1- a) Large-scale map of Greater Anatolia showing major faults and tectonic plate arrangement (Şengör et al., 1985; Çiner et al., 2015), b) Regional geology of the central smCAP. The yellow box highlights the Attepe region shown in c) Geological map of the Attepe iron deposits (Keskin, 2016). Formation descriptions in stratigraphic column (Figure 2). EAP – East Anatolian Plateau, AMP – Anatolian microplate, NAF- North Anatolian fault, CAFZ – Central Anatolian fault zone, WAEP – Western Anatolian extensional province, IA – Isparta Angle, PT – Pliny trench, CA – Cyprus Arc, EF – Ecemis fault zone, EAF – East Anatolian fault, DSTF – Dead Sea transform fault, BZS – Bitlis-Zagros suture.

of the Taurides and its influence on regional climate, especially the timing of aridification of the CAP, is contentious.

Stable isotope records of lacustrine carbonates across the CAP record a relatively humid climate in the Mut Basin/Ecemis Corridor regions from the late Oligocene to early Miocene (Lüdecke et al., 2013). Although by the early Miocene the CAP was not yet bordered by orographic barriers to the north and south, the depositional environment had shifted from

large, open freshwater lakes to smaller closed saline lakes despite high humidity (Lüdecke et al., 2013). The lack of significant pre-Miocene orographic rain-out has been recognised in the $\delta^{18}O$ composition of carbonates from large continental basins, although the data point to the onset of uplift and establishment of an orographic barrier by 5 Ma (Lüdecke et al., 2013; Keskin, 2016; Meijers et al., 2016, 2018). Throughout the late Miocene the smCAP drained internally, however it was connected to the Mediterranean Sea in the early Pliocene (Meijers et al., 2020). Around the easternmost Mediterranean Sea, underplating of material derived from the African plate during progressive collision with the Anatolian plate led to uplift of marine sediments in the Adana basins, south of the Taurides, in the Late Messinian thus establishing drainage to the Mediterranean Sea and resulting in the deep incision of the Taurides (Jaffey and Robertson, 2005). The initiation of uplift across the smCAP in late Miocene is suggested to reflect lithospheric slab break-off and subsequent asthenospheric upwelling and perhaps the arrival of the Eratosthenes Seamount at the collision zone to the south of Cyprus. (Cosentino et al., 2012; Schildgen et al., 2012; Radeff, 2014; Schildgen et al., 2014).

Meijers et al. (2020) proposed that a sub-humid Anatolian climate persisted during late Miocene surface uplift, and that the smCAP was relatively low relief with stable (>1 Ma) palaeoenvironmental and hydrological conditions during CAP uplift based on the stable isotope composition of lacustrine carbonates. Delayed aridification of the CAP and its southern margin was potentially caused by an increase in mean annual precipitation into the Pliocene (Kayseri Özer, 2017). The Quaternary marine terraces along the smCAP allowed Racano et al. (2020) to develop a landscape evolution model suggesting that the mountain belt was essentially formed during a pulse of rapid uplift (1.9 to 3.5 m/kyr) between 500 and 200 kyr that resulted in 1.5-2 km of surface uplift (Racano et al., 2020). This is supported by Öğretmen et al. (2018) who use the occurrence of middle Pleistocene benthic fauna, indicative of an epibathyal marine environment, now identified along the smCAP on a palaeocoastline at ~1500 m above sea level to suggest a short-lived pulse of rapid uplift (3.2-3.4 m/kyr) since the middle Pleistocene (~450 kyr). This implies that the modern topography and the orographic barrier along the smCAP was established in the last 500 kyr.

Fe-oxides and-oxyhydroxides (Fe-O) are ubiquitous near surface weathering products formed during relatively wet humid climates (Tardy and Nahon, 1985; Monteiro et al., 2014; Vasconcelos et al., 2015; Deng et al., 2017; Monteiro et al., 2018). Modest U and Th concentrations in Fe-O minerals can produce measurable ^{4}He by radioactive decay. At the surface temperatures the diffusion rate of He within Fe-O minerals is low enough that it is quantitatively retained and the (U-Th)/He ages can be used to determine the timing of mineral precipitation (Schuster et al., 2005). Consequently, He ages for Fe-O are now widely used to determine when climate conditions were conducive to supergene mineralisation (Vasconcelos et al., 2015). Vasconcelos et al. (2015) have proved useful for constraining how and when tectonic uplift initiates a change in climate, for example, the onset of aridity in the Central Andes (Cooper et al., 2016) and changes to Asian monsoon dynamics (Deng et al., 2017).

The Attepe iron deposits lie on the northern fringe of the smCAP in the western part of the Eastern Taurus mountains at more than 1.5 km above sea level (Figure 1). Over 90% of iron production is concentrated in thick oxidised zones in the upper part of deposits (Küpeli, 2010; Keskin, 2016; Keskin and Ünlü, 2016*a*; Keskin and Ünlü, 2016*b*; Keskin and Ünlü, 2016*c*; Keskin and Ünlü; 2021). They are dominated by limonite and goethite that were formed by supergene alteration and poly-phase karstification during wet humid climate regime (Küpeli, 2010). The current cold, semi-arid climate of the region is not conducive to supergene oxidation. Consequently, dating the supergene alteration of the Attepe deposits has the potential to constrain the timing of climate change in the Taurides. Here, we present (U-Th)/He ages of fully characterised supergene Fe-O mineralisation from four mines within the Attepe district in order to determine when climate conditions on the smCAP were conducive to supergene enrichment and when the cold semi-arid climate of today were established.

2. Geological setting

The Taurus Mountain range extends over 1500 km across from southern Türkiye to Iran. They record a complete plate-tectonic cycle beginning with rifting, followed by seafloor spreading, and final collision of African and Eurasian plates during the late Mesozoic to early Cenozoic (Robertson, 2007). It is widely accepted that they are composed of continental fragments that were rifted from North Africa during the opening of the southern Neotethys Ocean in the Mesozoic (Şengör and Yılmaz, 1981; Robertson and Dixon, 1984). The progressive closure of the southern Neotethys Ocean is associated with ophiolite emplacement during the late Cretaceous and ultimately closure by the Miocene (Robertson, 2007; Parlak et al., 2013). Further convergence resulted in the westward escape of the Anatolian microplate along the northern and eastern Anatolian fault zones from the mid-Miocene (Şengör et al., 1985; Bozkurt, 2001). This movement continues today with Anatolia undergoing counter-clockwise rotation and westward escape from Eastern Anatolia at a rate of ~30 mm/yr (Bozkurt, 2001). The Tauride Mountains are typically divided into the western, central, and eastern Taurides, with the latter located east of the Ecemis fault and being of primary interest to this study.

Middle to late Miocene marine fossil assemblages in the Dikme basin, located approximately ~10 km north west of the Attepe iron deposits, records the final marine incursion into the smCAP (Ocakoğlu, 2002). To the south-west, the 6.7 Ma marine sediments of the Mut-Ermenek Basin now lie at depths of 1.5-2 km, implying surface uplift rates of 200-300 m/Myr (Robertson and Grasso, 1995; Cosentino et al., 2012; Schildgen et al., 2012). This may have been initiated by the switch from crustal shortening to extension along the smCAP, linked to oceanic slab break off and tearing in middle to late Miocene (Schildgen et al., 2014). The surface exposure ages of strath terraces in the Mut basin reveal average uplift rates of 250 to 370 m/Myr since 8 Ma with periods of higher uplift rate of between 600 to 700 m/Myr after 1.66 Ma (Schildgen et al., 2012). From the early to middle Pleistocene period, the increase in uplift across southern Türkiye may have been caused by collision of between the Eratosthenes Seamount with the subduction trench where the African and Eurasian plates converge to the south of Cyprus (Schildgen et al., 2012).

The 10 km^2 Attepe mining district lies between 1.5 and 2 km above sea level on the western side of the Eastern Taurus Mountains in the Kayseri-Adana region of southern Türkiye (Figure 1) (Küpeli 2010; Keskin, 2016). It is one of Türkiye's most important Fe-ore producers, with reserves of up to 70 Mt and with an estimated 1 Mt of ore currently being extracted annually from the Attepe and Elmadağbeli mines at an average grade of 45-58 % Fe_2O_3 (Küpeli, 2010; Keskin and Ünlü, 2012; Keskin, 2016). The main ore hosting formations are present within the metasedimentary rocks of the 4 km thick Palaeozoic Geyikdağı Unit (Figure 2). Basement lithologies have undergone low-grade metamorphism with multiphase deformation occurring during the Caledonian, Hercynian, and Alpine orogenic events (Küpeli, 2010; Tiringa, 2016; Keskin, 2016; Keskin and Ünlü, 2016*b*; Keskin and Ünlü, 2021).

The oldest mineralisation phase comprises uneconomic syn-sedimentary pyrite and hematite, which are hosted in the metasedimentary and metavolcanic units of the Precambrian Emirgazi formation (Henden et al., 1978; Ayhan et al., 1992; Dağlıoğlu and Bahçeci, 1992; Dayan, 2007; Küpeli, 2010; Keskin and Ünlü, 2012; Keskin ve Ünlü 2016*c*). A later phase of Palaeocene to Lower Eocene hydrothermal-metasomatic vein-type iron carbonate mineralisation is hosted in Middle to Upper Cambrian dolomitic limestones within Değirmentas formation (Dayan, 2007; Küpeli, 2010; Tiringa, 2016; Keskin and Ünlü, 2016*c*) (Figure 3). The ore bodies occur as veins, lenses or stocks composed ankerite and siderite with associated hematite, chalcopyrite, tetrahedrite, pyrite and marcasite veins hosted in the Emirgazi, Cambrian Değirmentaş and Armutludere, and Jurassic Kızlarsekisi formations (Henden et al., 1978; Küpeli, 2010; Keskin, 2016). The mineralisation is controlled by NE-SW and ENE-WSW trending fault systems which provided pathways for hydrothermal fluid flow, and most economic deposits occur where fault systems interact (Keskin and Ünlü, 2012; Keskin, 2016; Keskin and Ünlü, 2021).

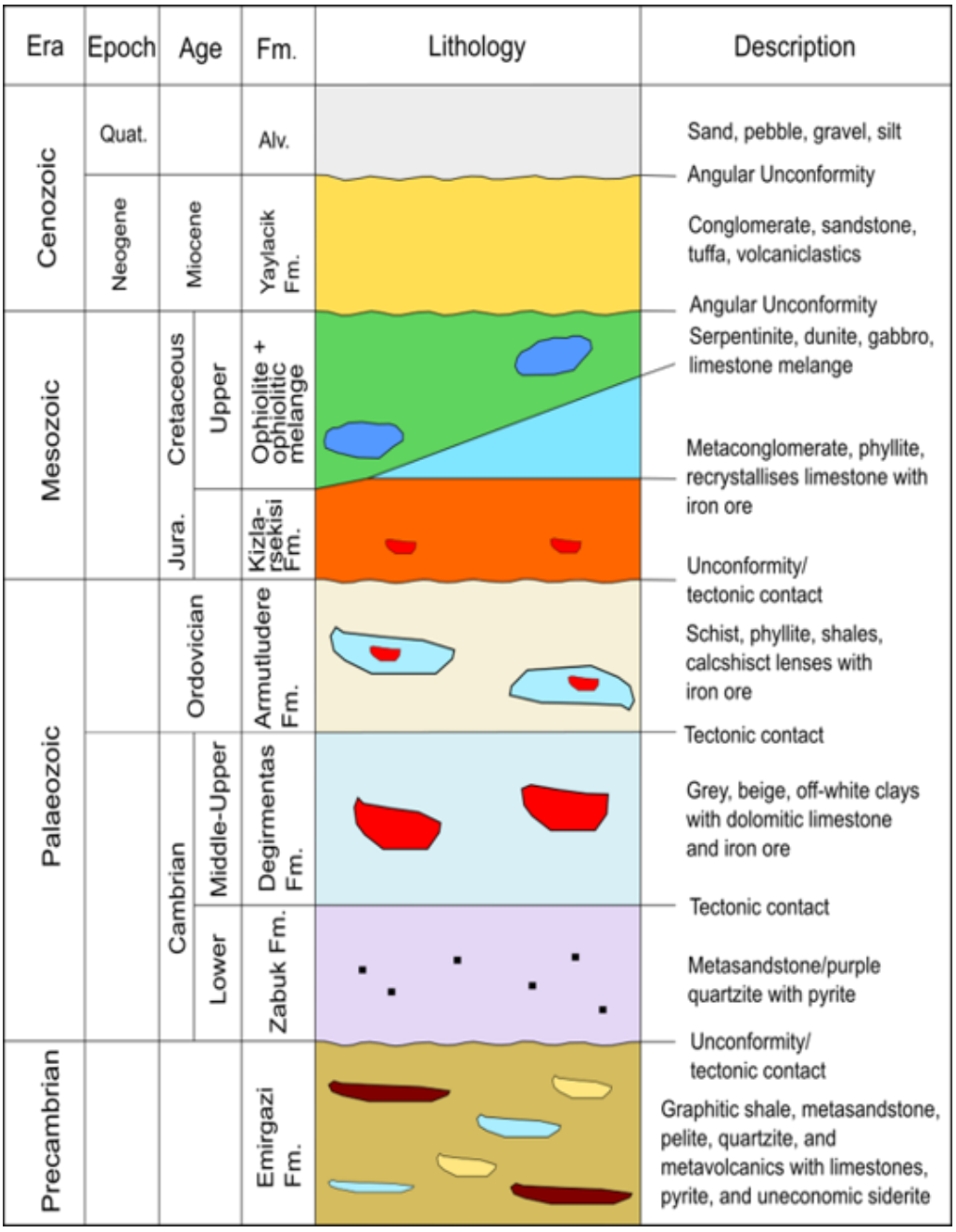

Figure 2- Stratigraphic column showing the main geological units across the Attepe ore deposits (Modified from Keskin, 2016).

The hydrothermal-metasomatic mineralisation has been subjected to extensive supergene alteration, known as karstic Fe-oxi-hydroxide (KIO) mineralisation (Küpeli et al., 2007, Keskin et al., 2010). It is evident from the 20-30 m thick zones of dominantly limonite, goethite, and hematite, with less abundant malachite, azurite, lepidocrocite, manganite and calcite.

The oxidation zones in each mine are not laterally or vertically consistent over the entire ore deposits (Küpeli et al., 2007, Figure 4). Supergene-enriched ores tend to replace the vein-type ores along faults and fracture systems as opposed to a homogeneous, stratified weathering front. In the field, the oxidation zones are recognised as intensely weathered friable rock, boxwork textures, and occurrences of massive

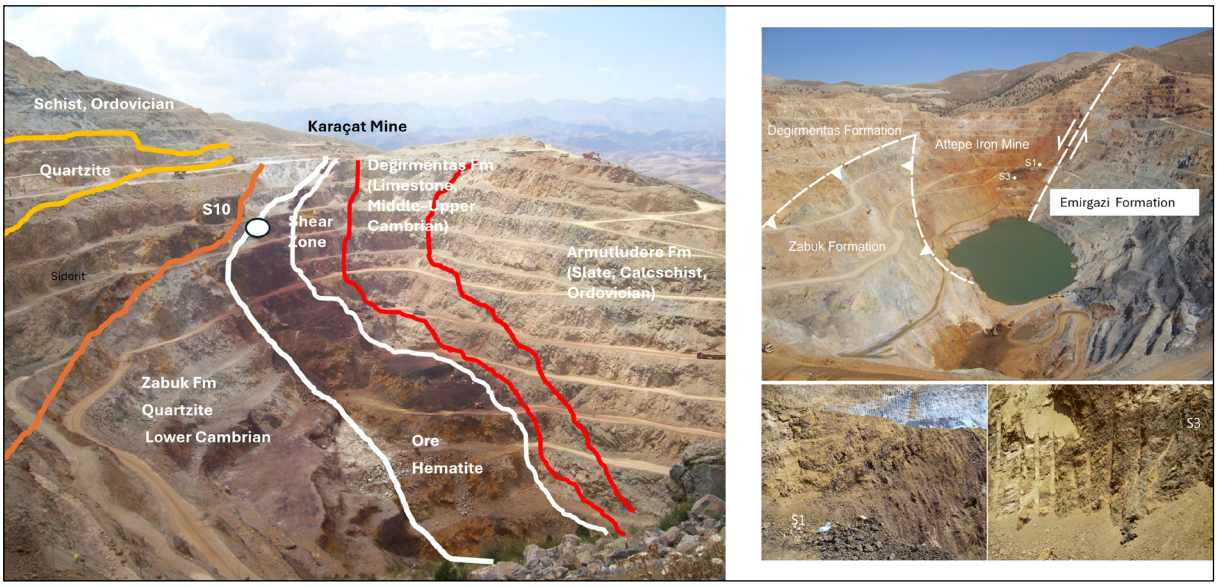

Figure 3- Attepe and Karaçat Iron Deposits and some location of samples (1,3,10).

botryoidal goethite. The oxidation phase is the dominant source of iron ore in the Attepe mining district, accounting for more than 90% of the extracted iron (Küpeli, 2010). The Attepe Mine is the largest and most economically important, extending over 500 m long and in places up to 200 m deep (Küpeli, 2010; Tiringa, 2016; Keskin, 2016, Figure 4).

The current climatic conditions of the CAP, further north of the Attepe iron deposits, are classed as semi-arid; mean summer temperatures of 23°C, mean winter temperatures of -2°C, mean annual precipitation <500 mm (Schemmel et al., 2013). Modern climate records for the Niğde, located approximately ~80 km west of the Attepe iron deposits, at an elevation

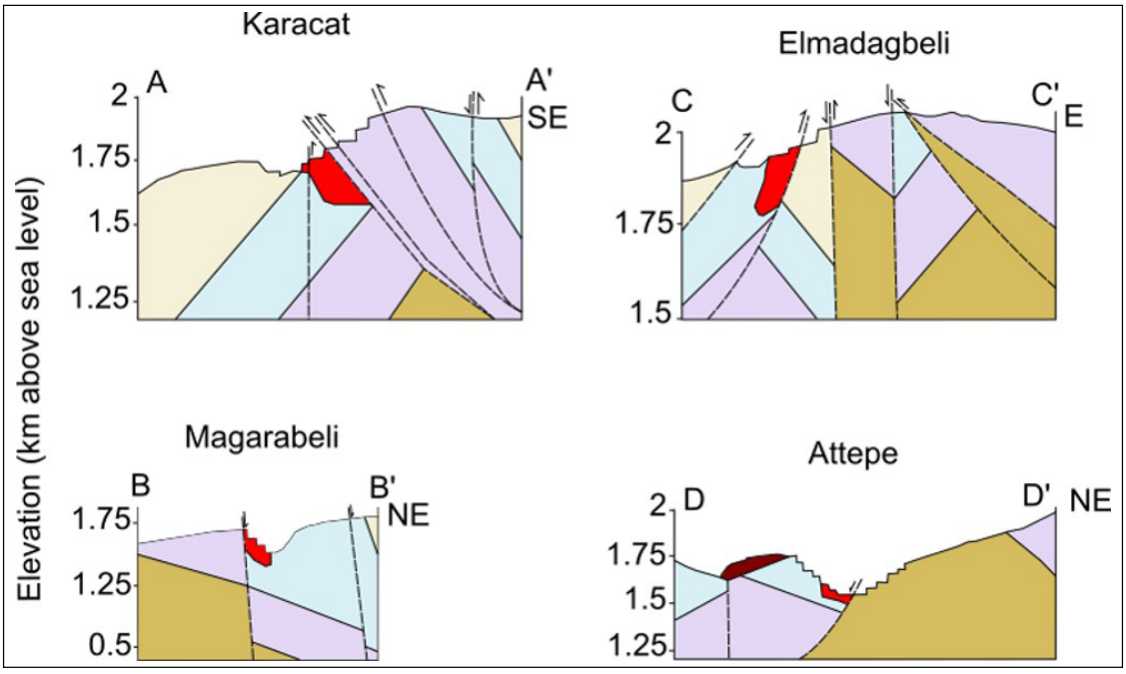

Figure 4- Cross sections of each mine showing relationship to main lithologies and faults. Cross section lines are taken from Figure 1c in main text (Revisied from Keskin, 2016)

of around ~1300 m above sea level, records a cold semi-arid climate (mean summer 20.5°C, mean winter temperatures of 4.3°C, mean annual rainfall typically <350 mm) with hot dry summers, cold and often snowy winters, and 90 % precipitation falling between autumn and spring and only 10 % of it occurs summer (Sarıkaya et al., 2015). To the south of the smCAP, a mild Mediterranean climate prevails (mean summer temperatures of 29°C, mean winter temperatures of 9°C and, mean annual rainfall typically >1000 mm) (Şensoy, 2004).

3. Sample descriptions

We have analysed seven Fe-O samples from four mines; Attepe, Mağarabeli, Karaçat and Elmadağbeli. These samples were taken from within the supergene zone of active mine operations; where availability was governed by accessibility. Then, the samples were dried and gently crushed. After that, 1-2 mm chips free of gangue minerals were picked, crushed, and sieved. Next Gangue minerals, predominantly calcite and quartz, were removed from the 0.25-1 mm fraction using a Frantz LB-1 magnetic separator and hand-picking under binocular microscope. This fraction was re-crushed and gangue minerals removed from the 150-250 µm fraction. A final crush step using a quartz-agate pestle and mortar was used to produce a <38 µm fraction for powder X-ray diffraction (XRD), He, U, and Th determinations.

XRD was carried out using a Panalytical X'Pert PRO MPD (A3-26) at School of Chemistry, University of Glasgow. The diffractometer is equipped with a Cu target tube operated at 40 kV and 40 mA and was set to scan between 10 and 60° 2θ scan range with a step size of 0.017° with each step taking between 60-150 seconds. The mineral composition has been determined for all samples; samples S1, S3, and S11 are pure goethite, S4 and S8 are hematite-goethite mixtures, S9 is a mixture of hematite with minor magnetite (Fe_3O_4) and S10 is hematite only. No minor phases were present above detection limit (<1%) (Table 1).

By applying the Scherrer equation to each sample diffractogram result, the average crystallite size (or mean coherent domain size) for each sample was obtained (Figure 5, Table 1). Average crystallite sizes range from 28 ± 10 nm to 84 ± 2 nm. Between them, pure goethite samples tend to record greater average crystallite size; Crystallite size is generally taken as the cube root of the volume of a crystallite and, using the Scherrer equation to calculate it, provides a lower estimate of crystallite size since the effects of strain and crystal lattice imperfections on peak width are not considered (Speakman and Shackley, 2013). Further, if sample material has average crystallite size <100 nm, it is taken as the thickness of the crystallite analysed (Monshi et al., 2012). Crystallite size is not necessarily grain size, since grains can be composed of many crystallites (Taylor, 2011; Moshi, 2014; Monterio et al., 2014). This method for crystallite size estimation allows for the correction of diffusive loss of He from Fe-O, like in Allard et al. (2018). However, Allard et al. (2018) use Rietveld refinement prior to calculation of crystallite size which accounts for strain and crystal lattice imperfection.

Rock chips up to 5 mm^3 were imaged using a FEI Quanta 200F environmental scanning electron microscopy (SEM) operated at 20 kV at the ISAAC facility, University of Glasgow (Lee et al., 2014). All samples are poly-crystalline, show boxwork texture with many crystal forms (e.g. botryoidal, prismatic, needle-like, fibrous or platy) being present in all samples (Figure 6). Crystal dimensions range from 0.1 µm to 300 µm and typically make up larger aggregates of crystals or form ribs in the pervasive boxwork texture. Colloform banding is present in sample S3 which provides evidence of progressive crystallisation from a fluid phase into open spaces (Figure 6, Figure 7). Small pyrite (Figure 6n) and Pb-Ca phosphate mineral inclusions are visible in SEM (Figure 6e-f). SEM and BSE analyses conducted several samples that given only S3 and S10 samples figures (Figure 7 and Figure 8).

4. Analytical procedures

In order to avoid problems associated with the volatilisation of U and Th during the heating (800-1000°C) required for He extraction (e.g. Vasconcelos et al., 2013; Hofmann et al., 2020), we have determined He separately from U and Th in multiple aliquots of several mg of each sample. This data was

Table 1- XRD diffractogram data from iron oxide/oxyhydroxide samples from the Attepe iron deposits, Türkiye.

Sample	Mineralogy	Relative Intensity (%)	FWHM (degrees)	FWHM (radians)	Peak Position (degrees)	Peak Position (radians)	D	D average	stdev	error (%)
S1	FeOOH	100	0.1428	0.0025	21.1	0.2	59.1	72.2	22.9	41.4
	FeOOH	48	0.0816	0.0014	33.1	0.3	106.1			
	FeOOH	69	0.102	0.0018	36.6	0.3	85.7			
	FeOOH	33	0.2448	0.0043	53.1	0.5	37.9			
S3	FeOOH	100	0.1428	0.0025	21.1	0.2	59.1	65.6	30	45.7
	FeOOH	78	0.1632	0.0028	36.5	0.3	53.5			
	FeOOH	49	0.1428	0.0025	33.1	0.3	64			
	FeOOH	33	0.204	0.0036	40.8	0.4	37.9			
	FeOOH	31	0.0816	0.0014	58.7	0.5	116.7			
S4	Fe_2O_3	100	0.2856	0.005	33.1	0.3	30.3	27.6	10	36.2
	Fe_2O_3	88	0.204	0.0036	35.6	0.3	42.7			
	FeOOH	63	0.4896	0.0085	54	0.5	19			
	FeOOH	32	0.4896	0.0085	40.8	0.4	18.1			
	Fe_2O_3	31	0.3264	0.0057	49.4	0.4	28.8			
S8	Fe_2O_3	100	0.2856	0.005	33.1	0.3	30.3	27.9	4.4	15.7
	Fe_2O_3	57	0.2856	0.005	35.6	0.3	30.5			
	FeOOH	52	0.408	0.0071	53.9	0.5	22.8			
S9	Fe_2O_3	100	0.204	0.0036	32.8	0.3	42.4	40.1	2.9	7.1
	Fe_3O_4	78	0.204	0.0036	35.3	0.3	42.7			
	Fe_2O_3	61	0.2448	0.0043	53.7	0.5	38			
	Fe_2O_3	38	0.2448	0.0043	49.1	0.4	37.3			
S10	Fe_2O_3	100	0.2244	0.0039	33.1	0.3	38.6	34.5	5.7	16.5
	Fe_2O_3	61	0.2856	0.005	35.6	0.3	30.5			
	Fe_2O_3	57	0.2448	0.0043	54	0.5	38			
S11	FeOOH	100	0.102	0.0018	21.2	0.2	82.8	84.4	1.5	1.8
	FeOOH	48	0.102	0.0018	33.2	0.3	84.9			
	FeOOH	68	0.102	0.0018	36.6	0.3	85.7			
							Average D (nm)	50.3	23.3	46.20%

Scherrer Equation $D = k \times \lambda / \beta (\cos\theta)$

D = crystallite size (nm)

k = Scherrer's Constant (for spherical crystallites with cubic symmetry) 0.94

λ = x-ray wavelength Cu K-alpha 1.5406; or 0.15406 Å (Angstrom)

β = FWHM (Full Width Half Maximum in radians - peak width)

θ = peak position (radians) 0.5

used to calculate an average He concentration and average U and Th concentration for each sample, which were used to determine the sample (U-Th)/He age using the formulation of Meesters and Dunai (2005). This procedure has been used successfully to date hematite mineralisation from Elba yielding ages that are indistinguishable from Ar/Ar ages of cogenetic adularia (Wu et al., 2019). The technique used here differs from the standard technique where multiple single aliquots are dated, which often yields over-dispersed age populations (e.g. Cooper et al., 2016; dos Santos Albuquerque et al., 2020, Figure 9).

Helium analysis procedures were identical to those of Wu et al. (2019). For each sample we analysed He in 6-9 aliquots. Between 3 and 9 mg of <38 μm fraction were weighed into Pt-foil packets. Typically, four sample aliquots and one empty packet

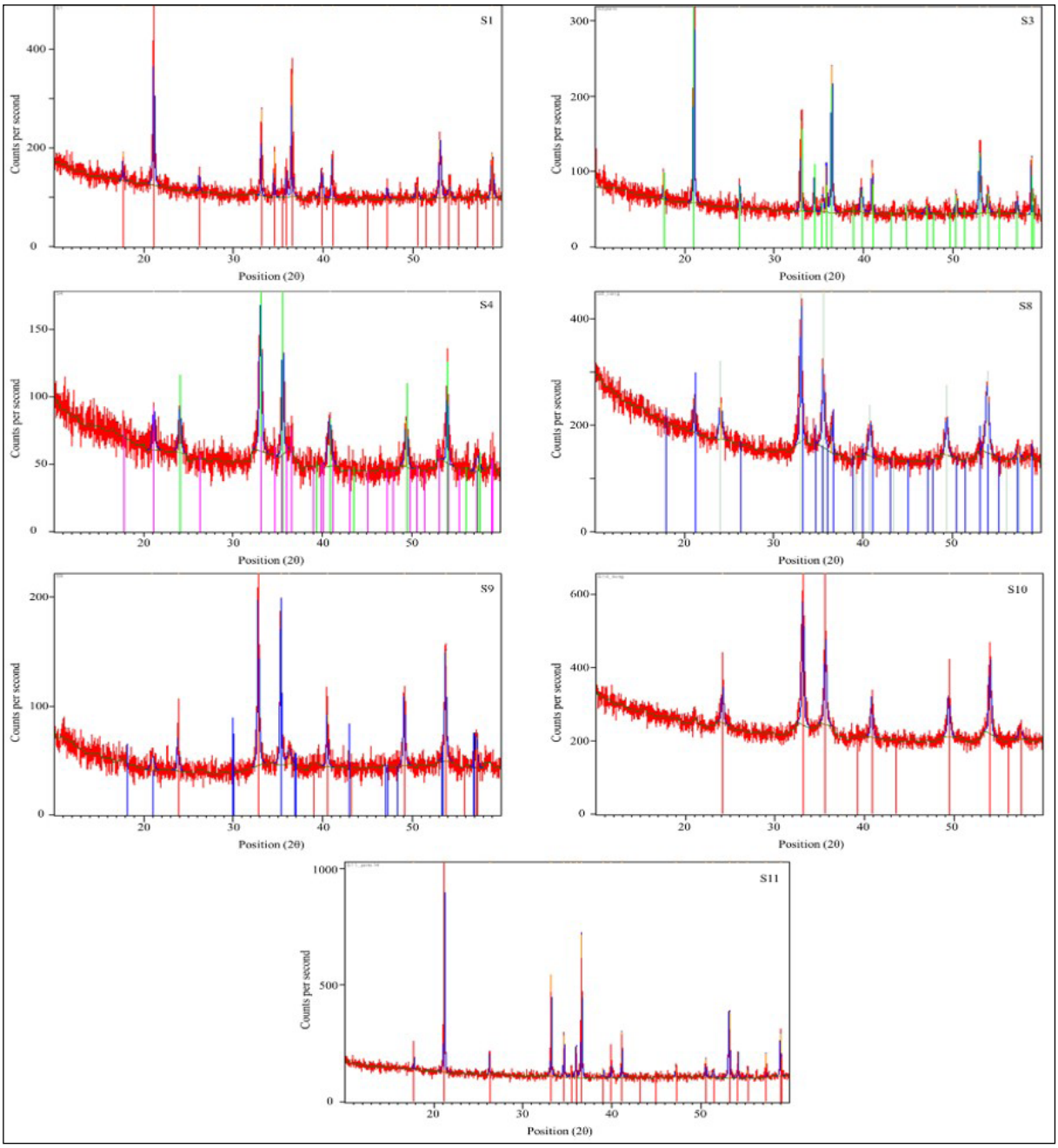

Figure 5- Diffractograms of each sample. S1: Highest intensity peak recorded at 21.1θ indicative of goethite. S3: Highest intensity peak recorded at 21θ indicative of goethite. S4: Highest intensity peak recorded at 31.1θ indicative of hematite, with goethite a minor component recording 63 % and 32 % relative peak height (violet lines under diffractogram) and < 20 nm crystallite size. S8: Highest intensity peak recorded at 31.1θ indicative of hematite, with goethite a minor component recording a 52 % relative peak height (blue lines45 under diffractogram) and 22 nm crystallite size. S9: Highest intensity peak recorded at 32.8θ indicative of hematite, with magnetite recording a 78 % relative peak height at 35.3θ (blue lines under diffractogram). S10: Highest intensity peak recorded at 31.1θ indicative of hematite. S11: Highest intensity peak recorded at 21.1θ indicative of goethite.

were placed 10 mm apart in recesses in a degassed Cu pan and covered with a sapphire window prior to overnight pumping at 80°C to minimise background levels of H and CH_4. Helium was extracted by heating the Pt packets to 1000 ± 20°C for 300 seconds using a 960 nm diode laser heating system (Fusions 960, Photon Machines). Laser power was regulated using the inbuilt pyrometer which maintained sample

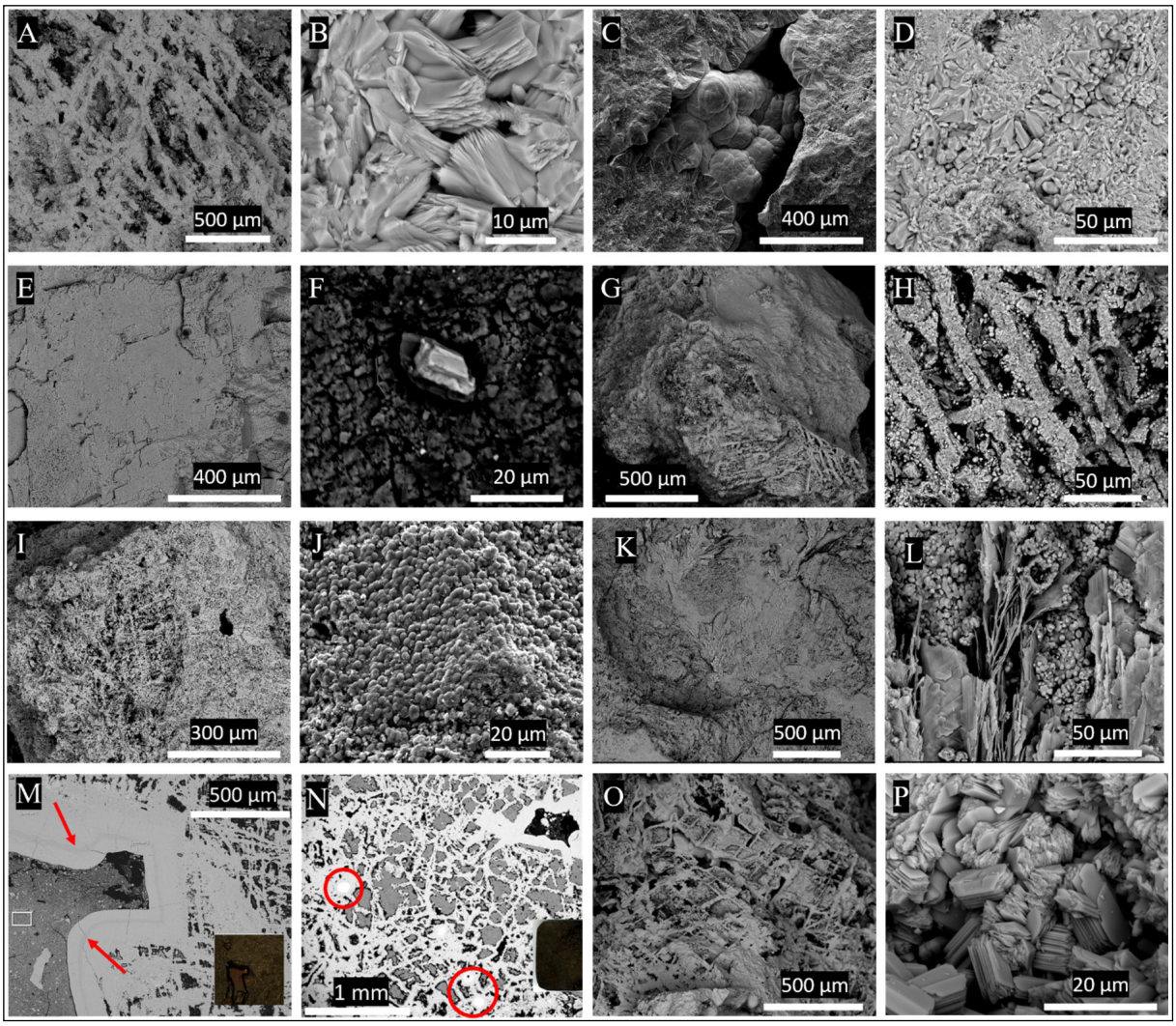

Figure 6- Back-scattered electron SEM images of supergene iron oxyhydroxide textures from the Attepe iron ore deposits, a) S1: Boxwork texture with protruding ribs and hollowed central section, b) S1: Plate-like morphology of goethite crystals within rib of boxwork texture, c) S3: Botryoidal goethite filling open-space, d) S3: Poly-crystalline goethite with prismatic, needle-like, and platy crystal morphology. Boxwork ribbing is typically composed of plate-like and prismatic morphology whereas hollowed central sections are primarily filled with needle-like goethite, e) S4: Pitted and weathered platelets of hematite and goethite with pits potentially due to radiation damage from a Pb-Ca phosphate phase, f) S4: PbCa phosphate phase, with an apparently hexagonal habit, perhaps phosphohedyphane, or another pyromorphite-group mineral within hematite-goethite matrix, g) S8: Fractured chip highlighting pervasive boxwork texture, h) S8: Boxwork texture with fibrous masses of hematite and goethite coating the outer surface of ribs and growing into open spaces, i) S9: Chip exhibiting boxwork texture and multiple open spaces, j) S9: Reniform masses of hematite coating a surface on the sample, k) S10: Boxwork and dendritic textures in hematite, l) High magnification image of dendritic platy hematite alongside reniform balls of hematite, m) S3: Red arrows show younging direction of colloform banding suggesting progressive crystallisation from fluid into open space, n) S3: red circles show <100 µm blebs of pyrite within boxwork texture S11: Boxwork texture in goethite, n) S11: Plates of goethite which form the ribs of boxwork texture.

temperature. All sample tubes were re-heated to ensure complete He extraction. Sample re-heats released on average 0.2% of the initial He and were not used in He concentration determinations. The evolved gases were purified for 600 seconds using a combination of hot and cold SAES TiZr getters and two liquid nitrogen-cooled charcoal traps. Helium abundances were determined using a Hiden HAL3F quadrupole mass spectrometer operated in static mode (Foeken et al., 2006). Absolute ^{4}He concentrations in samples were calculated by peak height comparison against repeated measurements of a calibrated He standard. Blocks of standard determinations were carried out before and after every two sample aliquots. Within

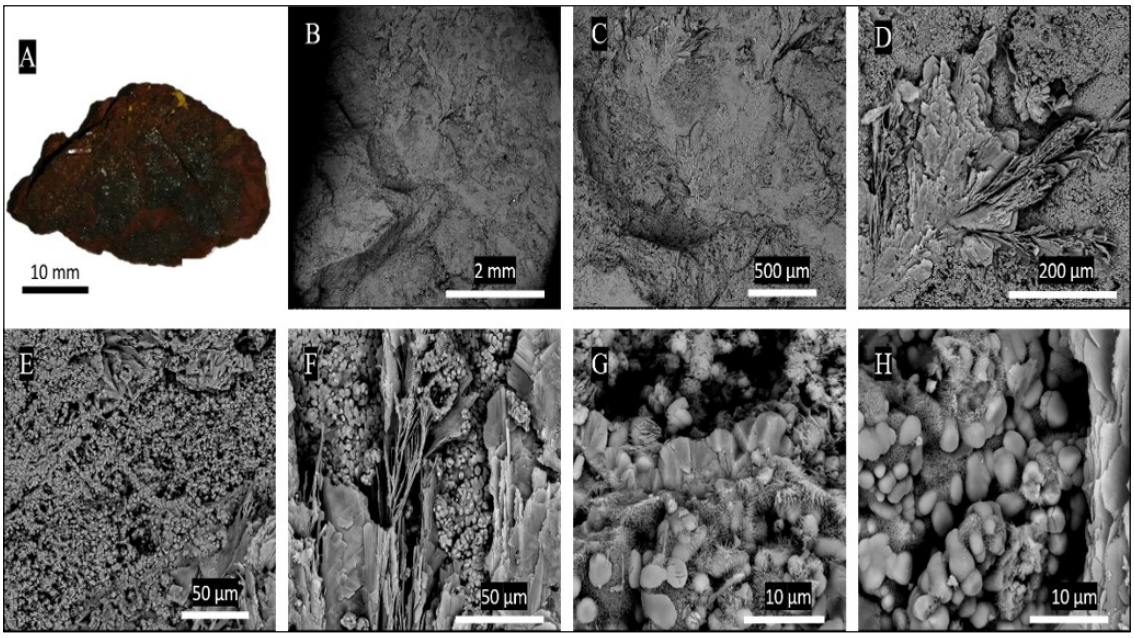

Figure 7- Representative hand sample and back-scattered electron (BSE) SEM images of sample S3 from the Attepe mine, a) polished block, b) fresh surface of a chip liberated from larger sample. Metallic grey of goethite with friable yellow weathering evident, c) BSE image of image A showing boxwork texture of goethite, d) BSE image of image A showing colloform texture of goethite filling open/partially filled space. Boxwork texture on the inner surface of colloform banding (top, right, and bottom right of image) This implies that final boxwork development is synchronous with colloform banding, e) BSE image of broken chip showing botryoidal crystal morphology of goethite with botryoids filling open space, f) BSE image of broken chip showing boxwork texture, g) zoomed view of crystal morphology of goethite on the rib of boxwork texture. Crystals are typically prismatic or platy and 10 µm along c-axis, h) zoomed view of fibrous to platy morphology of goethite fringing hollows of the boxwork texture.

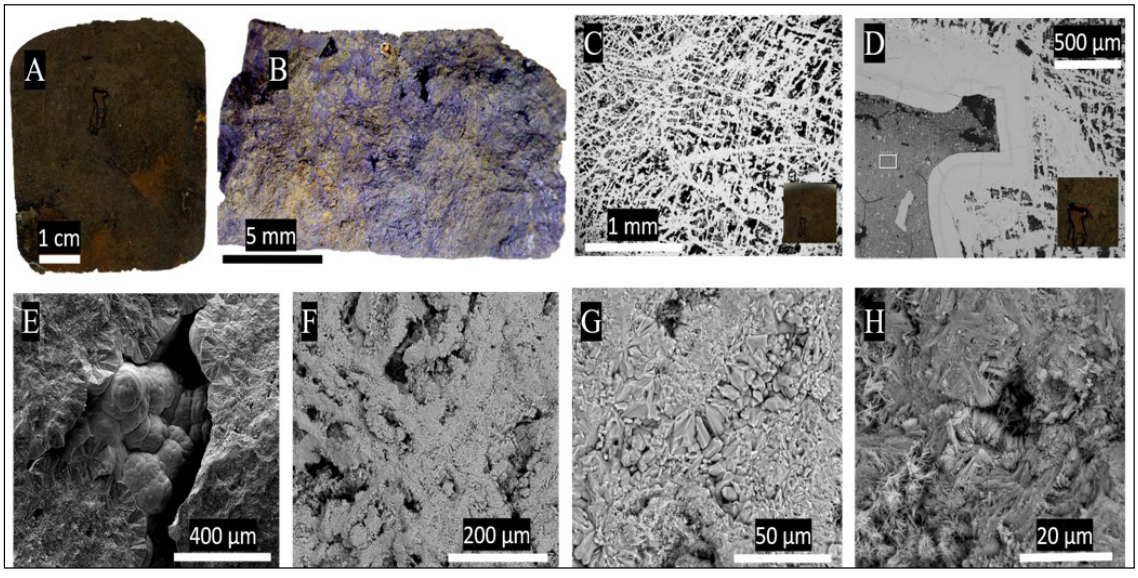

Figure 8- Representative hand sample and back-scattered electron (BSE) SEM images of sample S10 from the Karaçat Mine, a) hand sample showing fresher metallic hematite alongside red and yellow-orange weathered surfaces, b) BSE image of liberated chip showing boxwork and dendritic textures, c) zoom in on boxwork and dendritic textures showing rhombic ribbing structure, d) zoomed in dendritic texture with platy crystal morphology splaying from a central nucleus, Renifrom balls of hematite are interspersed within and alongside plates, e) zoomed in morphology of boxwork texture. Reniform balls combine to form the ribs with finer acicular crystals fringe the ribs into adjacent hollows, f) zoomed in dentritic plates of hematite alongside reniform hematite, g) zoomed in reniform hematite with fine acicular bladed hematite on the outer surfaces and within gaps, h) another angle of zoomed view of reniform hematite with fine acicular bladed hematite on the outer surfaces and within gaps with platy dentritic hematite on the right of image.

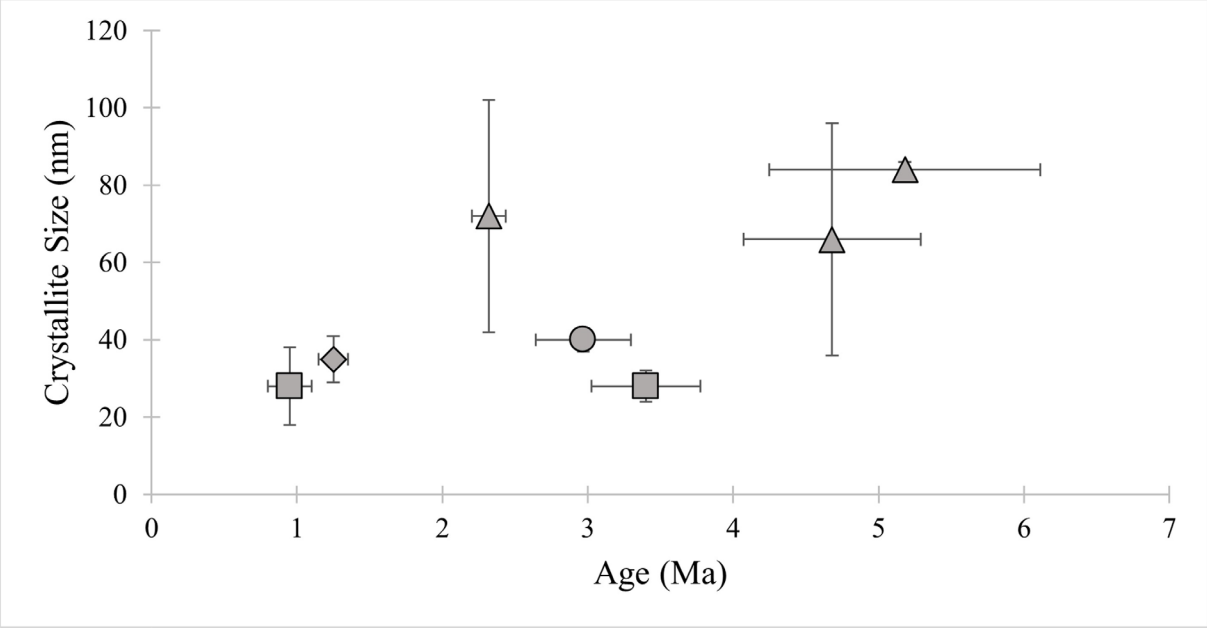

Figure 9- Age versus crystallite size and mineralogy plot. Triangle = goethite; circle = hematite/magnetite mix; square = hematite/goethite mix; rhombus = hematite.

these distinct analytical periods He sensitivity varied by ±1%. Helium blanks (3.6 x 10^{-11} ccSTP ± 73 %, n = 62) were determined by heating empty Pt tubes. Sample He contents were always more than 100 times the blank values (Figure 10).

Uranium and thorium concentrations were determined on 3-5 aliquots of 2-5 mg Fe-O samples. The sample dissolution procedures were essentially identical to those developed by Wu et al. (2019). U and Th were measured in Agilent 7500ce Q-ICP-MS. Blank levels were between 0.06 ± 0.05 ppm for U and 0.11 ± 0.10 ppm for Th. U and Th analysed in four aliquots of hematite (Italy-4) from the Rio Marina mine Elba yielded ^{238}U and ^{232}Th concentrations that overlapped values determined by Wu et al. (2019).

5. Results

^{4}He concentrations range from 0.49 to 8.3 x 10^{-10} ccSTP/mg (Table 1). Due to weighing error, blank corrections and variation in mass spectrometer sensitivity, individual He concentration determinations have an uncertainty of ±2 %. This is lower than the range of He concentrations measured in multiple samples (±4-7 %). The ^{238}U concentrations ranged from 0.07 to 1.55 ppm. Th was only measurable in four of the seven samples, with concentrations ranging from 0.01 to 0.19 ppm. The Th/U ratios of the four Th-bearing samples vary from 0.16-2.43 but are consistent within each sample. Single U and Th concentration determinations typically have an uncertainty of ±2 %. The effective uranium content within each sample (eU = [U] + 0.235 x [Th]) is ± 5 % in all but one sample.

The (U-Th)/He ages, which were calculated using the average He and eU concentrations for each sample, range from 0.90 to 5.08 Ma (Figure 10). Consistent with other studies of Fe-O (e.g. Shuster et al., 2005; Vasconcelos et al., 2013; Allard et al., 2018; dos Santos Albuquerque et al., 2020), no alpha ejection correction was applied. The total uncertainty of the sample He ages range from 5-18 % (1σ).

6. Discussion

6.1. Post-formation He loss

The diffusive loss of He from Fe-O can be significant at low temperatures and should be considered for when determining mineral crystallisation ages from (U-Th)/He data (Shuster et al., 2005; Vasconcelos et al., 2013; Allard et al., 2018). Helium diffusion rates are governed by mineral chemical composition and temperature, while the proportion of radiogenic

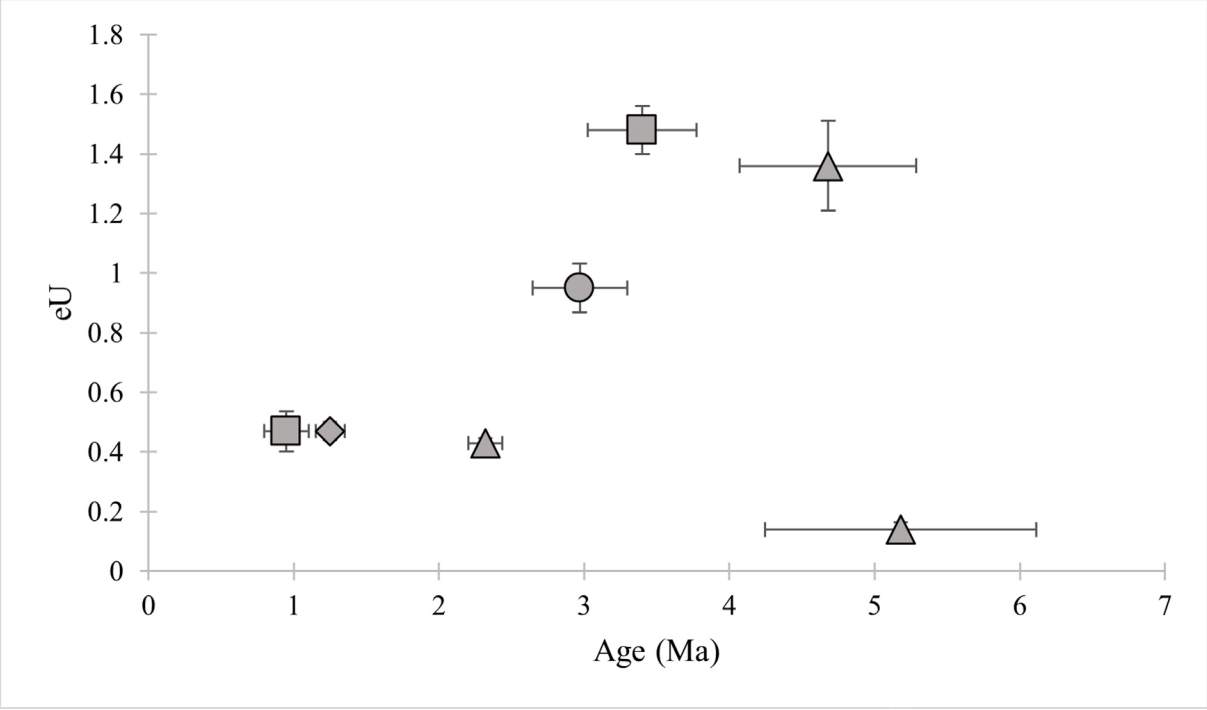

Figure 10- Age versus eU and mineralogy plot. Triangle = goethite; circle = hematite/magnetite mix; square = hematite/goethite mix; rhombus = hematite.

He lost from any sample is strongly dependent on mineral grain size (Farley, 2018). Where the deficit gas fraction has been determined on specific samples using the $^{4}He/^{3}He$ technique (e.g. Shuster et al., 2005; Heim et al., 2006; Deng et al., 2017), the percentage of He lost by diffusion can be constrained and corrected He age can be calculated. However, the parameters of He diffusion in the goethite and hematite are well established (Schuster et al., 2005; Farley, 2018) and the extent of He loss can be determined, and (U-Th)/He ages can be reconstructed, if mineral composition and grain size is known (e.g. Allard et al., 2018).

Helium diffusion in crystalline hematite is slow at low temperature (Bahr et al. 1994; Farley et al., 2018). For example, over 90 % of He is retained in 20 nm crystallites held at 30°C for 100 Ma, comparable to the He loss rate from 100 µm diameter apatite grains (Farley, 2018). Goethite is typically composed of poly-crystalline aggregates of varying properties and the more open crystal structure results in faster He diffusion. Shuster et al. (2005) showed that goethite contains regions with distinct He retention properties termed low resistivity domains (LRD), which likely account for most of the diffusive loss of ^{4}He. Extrapolating the data derived from $^{4}He/^{3}He$ analysis they showed that 3 to 10% of the He is lost at 25°C (Shuster et al., 2005). These distinct retention domains have been recognised in subsequent studies (Heim et al., 2006; Vasconcelos et al., 2013; Deng et al., 2017). By incorporating the crystallographic characterisations of goethite from ferruginous duricrust into the He production-diffusion code HeFTy (Ketcham, 2005), Allard et al. (2018) were able to simulate He retention in spherical domains of different radii. Using the diffusion coefficients of Shuster et al. (2005) and Vasconcelos et al. (2013) they determined that 10 to 25% of He is lost from 20 nm and 13 nm diameter goethite crystallites respectively at 25°C.

The crystallite-size of the samples in this study makes them susceptible to He loss, necessitating a correction to the (U-Th)/He ages (Figure 11). Assuming the maximum diffusion coefficient (D_o) value of 10 (Shuster et al., 2005; Vasconcelos et al., 2013), adopting the relationship between D_o and crystallite size defined by Allard et al. (2018) and using the mean crystallite size of samples determined by XRD, we can determine an upper limit on the proportion of He lost. Using this technique, we have

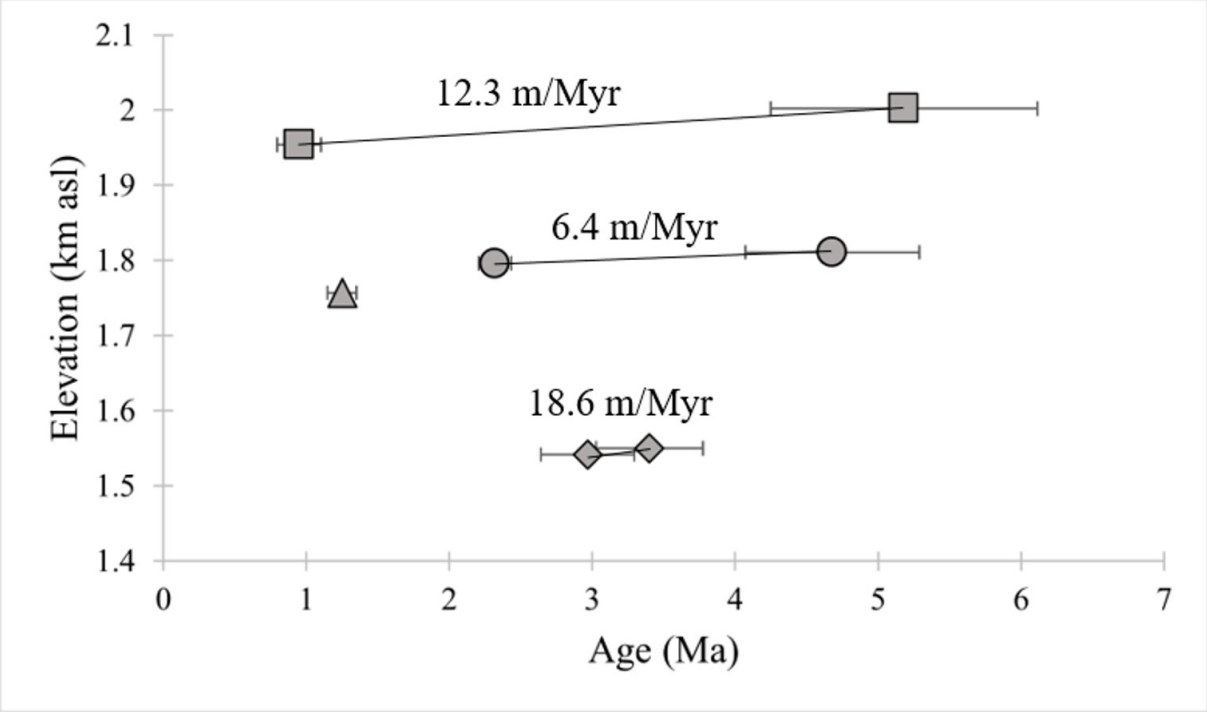

Figure 11- Age versus elevation plot of Attepe iron deposit samples with uplift/incision rates for each pair given above. Square = Elmadagbeli mine. Circle = Attepe mine. Diamond = Magarabeli mine.

calculated that the goethite samples (S1, S3, and S11) have lost up to 6 % of their He. The age correction for the mixed hematite-goethite samples (S8 and S4) has been determined based on the proportion of goethite as measured by XRD, and this also does not exceed 6 %. Sample S10 from the Mağarabeli mine is essentially pure hematite and requires an age correction of up to 4 %. Diffusion-correction suggests that the upper age limit (0.95 ± 0.15 to 5.18 ± 0.95 Ma) is not significantly different from the uncorrected ages, and that the age differences are within the analytical uncertainty (Table 1). There is no relationship between age and crystallite size, mineralogy or eU.

6.2. Unravelling climate and uplift history of the smCAP

The earliest preserved supergene phase is goethite from the Elmadağbeli deposit, the highest sample studied at 2002 m above sea level, which formed at 5.18 Ma. The latest supergene phase is S4 (0.95 Ma) the lower sample from the Elmadağbeli Mine (1994 m). In the three mines where two samples were analysed (Elmadağbeli, Attepe, and Mağarabeli) there is a systematic age increase with elevation (Figure 11). The age-depth relationships are typical of supergene profiles (e.g. Vasconcelos, 1999; Cooper et al., 2016; Deng et al., 2017), consistent with the downward migration of a weathering front related to lowering of the local water table. In a climate conducive to supergene enrichment, rock uplift and river channel incision can lower the water table independently of climate forcing, resulting in mineral precipitation age decrease with depth in a weathering profile (e.g. Deng et al., 2017). However, fluvial incision can be related to a switch to drier climate conditions, as suggested in the Chilean Andes (Cooper et al., 2016). Therefore uplift and a change in climate must both be considered as potential factors controlling the timing of Fe-O precipitation across the Attepe iron deposits.

The age-elevation relationship is not regionally consistent. The lowest altitude sample from the Attepe Mine (S1; 1796 m) is considerably younger than S8 from the Mağarabeli Mine despite it being from more than 200 m higher elevation (Figure 11). It is likely that faulting post-formation of the supergene profiles has changed the elevation of the studied profiles relative to each other (Keskin et al., 2010; Keskin ve Ünlü, 2016*a*, 2016*b*). Movement along the Ecemiş

Fault Zone (Figure 11), running NE-SW through the smCAP with ~60 km of sinistral displacement (Jaffey and Robertson, 2001), may have controlled local water table height variability. The Ecemis Fault Zone is a present-day seismic hazard and is one of Türkiye's most prominent fault zones (Yildirim et al., 2016). Movement on the Cevizlik Fault, ~60 km WSW of the Attepe iron deposits, has caused 13 m of vertical offset in moraine and talus fan surfaces in the last 22 ka, while the adjacent Kartal Fault records 120 m of vertical offset in the past 104 ka (Yıldırım et al., 2016).

The Attepe iron deposits lie on the northern edge of the smCAP. It is likely that they were already at significant elevation by the late Miocene (Schildgen et al., 2012; Cosentino et al., 2012; Schildgen et al., 2014; Radeff, 2014) with an emergent orographic barrier in close proximity (Lüdecke et al., 2013; Meijers et al., 2016; 2018). It is suggested that the Dikme basin, 15 km to the NW of Attepe, has been above sea level since 14 Ma (Ocakoğlu, 2002) and that Miocene uplift had brought the basin to ~1.8 km elevation by 5 Ma (Meijers et al., 2018). This uplift would have caused drainage reorganisation (Jaffey and Robertson, 2005; Meijers et al., 2020) and driven the precipitation of Fe-O above the falling water table so long as the climate was conducive to supergene enrichment and uplift was ongoing.

The Fe-O age data are difficult to reconcile with the model of rapid rock uplift resulting in the Attepe region reaching its current elevation in the past 500 ka (Öğretmen et al., 2018; Racano et al., 2020). It would generate significantly younger He ages as the absence of an orographic barrier until 500 ka would have allowed hot-humid climate to have persisted across the region, resulting in continued precipitation of supergene minerals into the middle Pleistocene. The youngest ages of 1.25 ± 0.10 Ma and 0.95 ± 0.15 Ma do not reflect this. Further, if the majority of the surface uplift occurred in the past 500 ka, erosion/incision would have removed the supergene mineralisation recorded across the Attepe iron deposits. Thus, the preservation of 1-5 Ma supergene mineralisation implies that the Attepe region must have been at or close to current elevation prior to 500 ka.

The elevation-age relationships at Attepe and Elmadağbeli mines record average incision rates of induced lowering of the water table of 18.6 and 6.4 m/Myr between ~5 and 1 Ma (Figure 11). This is equivalent to less than 100 m of incision and are clearly inconsistent with the generation of the 1-2 km of uplift required for the current elevation since Late Miocene or Mid Pleistocene. This suggests that the bulk of surface uplift in this region must have occurred prior to the Late Miocene.

Higher average Miocene uplift/incision rates are reported elsewhere. Uplift of 250-370 m/Myr in the Late Miocene (8 to 5.45 Ma), 730 m/Myr from 1.66 to 1.62 Ma, and 600-700 m/Myr from 1.6 Ma have been recorded in the Mut Basin, ~250 km southwest of our study area (Schildgen et al., 2012). Doğan (2011) reported river incision rates of ~80 m/Myr from 2 Ma to present approximately 150 km to the northwest of the Attepe iron deposits, and within the CAP. By assigning terraces to marine isotope stages, Doğan (2011) infers that all terrace levels formed during eccentricity-driven climate change cycles. Uplift/incision rates were substantially less across the Attepe region compared to basins to the south of the Taurides but were closer to those within the CAP. This is in line with the suggestion that the Attepe region has remained at a relatively stable elevation since the latest Miocene and that climate induced uplift/incision may be a key driver in water table drawdown and Fe-O precipitation.

Late Miocene pollen records for the Kırşehir-Kızılok region, 200 km NW of our study area, reveal conditions conducive for supergene Fe-O enrichment; mean annual temperature of 17°C, with mean cold month temperatures of 8°C, mean warm month temperatures of 27°C, and mean annual precipitation of 1045 mm (Kayseri-Özer, 2017). The persistence of high precipitation/temperature/humidity climate regime into the Early Pliocene has been documented across Central and Eastern Anatolia (Kayseri-Özer, 2017). The earliest He age recorded in this study (5.18 ± 0.93 Ma) indicates that similar, or a potentially hotter and more humid climate regime existed at this time considering the region is farther south. Evidence of earlier supergene Fe-O mineralisation awaits a more detailed investigation.

The youngest supergene He ages (1.25 ± 0.10 Ma and 0.95 ± 0.15 Ma) from samples from the Karaçat

and Elmadağbeli mines record the latest supergene enrichment (Figure 11). They require the hot-humid climatic conditions across the region into the Pleistocene and imply that the current cooler and drier climate regime was established sometime in the last million years or so. This contrasts starkly with the prevailing view which consider that the onset of aridification across the CAP began by the Middle Pliocene due to uplift and reorganisation of drainage rather than climate change (Meijers et al., 2020). It is, however, consistent with $\delta^{13}C$ and fauna data from pedogenic carbonates and calcretes in the Cal Basin which record a shift from Pliocene sub-humid to Pleistocene arid climate (Alçiçek and Alçiçek, 2014). Soil stratigraphy and the occurrence of palygorskite and kaolinite in the Adana basin, ~150 km south of Attepe, indicate that the wet to dry climate transition occurred during the Pleistocene (Kapur et al., 1993). Further study revealed mean annual temperatures in the northern portion of the Adana Basin to be 21-23°C with the presence of palygorskite and tree, shrub, and grass vegetation suggesting a semi-arid climate between 782 and 250 ka (Kaplan et al., 2013). Using calcrete formations, Eren et al. (2008) echo the establishment of semi-arid climate in the northern Adana Basin between 782 ka and 250 ka. They suggest a mean annual temperature of ~18°C and mean annual precipitation of <300 mm/yr; similar in temperature yet more arid than that of today in that region (>600 mm/yr) (Eren et al., 2008). Alluvial fan deposits in the high elevation (>2 km) Ecemiş River drainage area, ~60 km to the west of the Attepe region, record major climate shifts between cooler glacial periods and warmer interglacial/interstadial conditions from ~136 ka until the Pleistocene-Holocene transition (Sarıkaya et al., 2015).

Continuous long-term terrestrial climate records of Eastern Mediterranean/Western Asia are sparse. By interpreting European Cenozoic cool-temperature tree flora, Svenning (2003) reveals vegetation still widespread today are those most tolerant of a cold growing season whilst those in the Mediterranean region are cold-sensitive but relatively drought resistant. The 1.35 Ma Tenaghi Phillippon pollen record in NE Greece records a major shift from ~650 ka towards greater aridity during interglacial periods (Tzedakis et al., 2006). They suggest that continental vegetation change may have been independent of high-latitude glacial-interglacial marine and ice sheet records and that changes may have been a direct result of a climate shift towards interglacial aridity (Tzedakis et al., 2006).

Lake Van sits to the north of the orographic barrier created by the Bitlis Massif at >1600 m asl in the Eastern Anatolian high plateau region (Litt et al., 2014). The pollen record of the interglacial periods over the past 600 ka record an increase in abundance of pine (more cold-resistant) over oak (thermophilous) species. Like in the Tenaghi Phillippon pollen record, the Lake Van record does not totally coincide with global marine and ice sheet climate records, particularly around the mid-Brunhes event (~430 ka) and marine isotope excursion 7 (250 ka), thus suggesting that obliquity/eccentricity/processional climate mechanisms may cause different responses within continental interiors (Litt et al., 2014). However, a general cooling and aridification trend is recognised, broadly consistent with global climate data in the past million year (Zachos et al., 2001; Lisiecki and Raymo, 2005).

7. Conclusions

Fe-O from the oxidation zone of the Attepe iron deposits in the Eastern Taurides, southern Türkiye yield He loss-corrected (U-Th)/He ages between 5.18 and 0.95 Ma (Figure 11). Mines with two samples show a decrease in age with elevation, which is typical of a downward-moving water table. The uplift/incision rates of between 18.6 to 6.4 m/Myr between 5 and 1 Ma across the Attepe iron deposits are markedly slower than those recorded to the south, suggesting that the region was already at or close to its current elevation by the Late Miocene. Uplift/incision rates are closer to climate-induced uplift/incision recorded within the CAP over the past 2 Ma. The presence of goethite throughout the iron ore deposits in the Attepe region indicates that the climate was hotter and more humid at that time. The latest goethite precipitation (0.95 Ma) suggest that hot-humid climate ceased across the region sometime within the last million years. The clear evidence for regional and global climate cooling implies that it, rather than surface uplift, was the main driver of aridification across

the region. The preservation of the Mio-Pliocene supergene Fe-oxide-oxyhydroxide makes it unlikely that the region underwent rapid uplift in the last 500 ka.

Acknowledgements

We are very thankful to Isotope Geosciences, Scottish Universities Environmental Research Centre for analyses. Peter Chung, Marli de Jongh, Dr. Claire Wilson, Dr. Luigia de Nicola, and Dr. Valerie Olive are thanked for their assistance with SEM, XRD, He and ICP-MS analysis. We are grateful to Dr. Domokos Gyore and Dr. Marta Zurakowska for day-to-day discussion and practical assistance with laboratory matters. Dr. John Faithfull is thanked for discussions regarding mineralogy. We are also grateful to MTA (project number:2008-32-13-02.a) for supporting to this study. I dedicate this article to my PhD supervisor, Prof. Dr. Taner Ünlü (Ankara University), who passed away one year ago. I am deeply indebted to my professor, who has made significant contributions to my academic and personal development. His memory will remain with me forever, and his principles will be passed on to future generations through me. I would like to express my sincere gratitude to Dr. David Currie and Prof. Dr. Finlay M. Stuart for conducting most of the analyses in this study and for their contributions throughout the entire process. We had to publish this in memory of my supervisor. I am truly grateful to them.

References

Alçiçek, H., Alçiçek, M. C. 2014. Palustrine carbonates and pedogenic calcretes in the Çal basin of SW Anatolia: Implications for the Plio-Pleistocene regional climatic pattern in the eastern Mediterranean. Catena 112, 48-55.

Allard, T., Gautheron, C., Riffel, S. B., Balan, E., Soares, B. F., Pinna-Jamme, R., Derycke, A., Morin, G., Bueno, G. T., Do Nascimento, N. 2018. Combined dating of goethites and kaolinites from ferruginous duricrusts. Deciphering the late Neogene erosion history of Central Amazonia. Chemical Geology 479, 136–150.

Allmendinger, R. W., Jordan, T. E., Kay, S. M., Isacks, B. L. 1997. The evolution of the Altiplano-Puna plateau of the Central Andes. Annual Review of Earth and Planetary Sciences 25(1), 139–174.

Ayhan, A., Küpeli., Ş., Amstutz, G. C. 1992. Attepe (Feke-Adana) Demir Yatağının Bitişindeki Pirit Oluşumları. MTA Dergisi 114, 85-94.

Bahr, R., Lippolt, H. J., Wernicke, R. S. 1994. Temperature-induced 4He degassing of specularite and botryoidal hematite: A 4He retentivity study. Journal of Geophysical Research: Solid Earth 99, 17 695–17 707.

Bozkurt, E. 2001. Neotectonics of Turkey–a synthesis. Geodinamica acta 14(1-3), 3–30.

Çiner, A., Doğan, U., Yıldırım, C., Akçar, N., Ivy-Ochs, S., Alfimov, V., Kubik, P. W., Schlüchter, C. 2015. Quaternary uplift rates of the Central Anatolian Plateau, Turkey: insights from cosmogenic isochron-burial nuclide dating of the Kızılırmak river terraces. Quaternary Science Reviews 107, 81–97.

Cooper, F., Adams, B., Blundy, J., Farley, K., McKeon, R., Ruggiero, A. 2016. Aridity induced Miocene canyon incision in the Central Andes. Geology 44(8), 675–678.

Cosentino, D., Schildgen, T. F., Cipollari, P., Faranda, C., Gliozzi, E., Hudáčková, N., Lucifora, S., Strecker, M. R. 2012. Late Miocene surface uplift of the southern margin of the Central Anatolian Plateau, central Taurides, Turkey. GSA Bulletin 124(1-2), 133–145.

Dağlıoğlu, C., Bahçeci, A. 1992. TDÇİ sahalarının (Attepe, Koruyeri, Mağarabeli) değerlendirme Raporu. MTA Derleme No: 9339, Ankara (unpublished).

Dayan, S. 2007. Adana-Mansurlu Attepe civarındaki demir yataklarının jeolojik, petrografik ve yapısal özelliklerinin incelenmesi. A.Ü. Fen Bilimleri Enstitüsü, Yüksek Lisans Tezi. 125 sf. Ankara.

Deng, X.-D., Li, J.-W., Shuster, D. L. 2017. Late Mio-Pliocene chemical weathering of the Yulong porphyry Cu deposit in the eastern Tibetan Plateau constrained by goethite (U–Th)/He dating: Implication for Asian summer monsoon. Earth and Planetary Science Letters 472, 289–298.

Doğan, U. 2011. Climate-controlled river terrace formation in the Kızılırmak Valley, Cappadocia section, Turkey: inferred from Ar–Ar dating of Quaternary basalts and terraces stratigraphy. Geomorphology 126 (1-2), 66-81.

Dos Santos Albuquerque, M.F., Horbe, A.M.C., Danišík, M. 2020. Episodic weathering in Southwestern Amazonia based on (U-Th)/He dating of Fe and Mn lateritic duricrust. Chemical Geology 553, 119792.

Ehlers, T. A., Poulsen, C. J. 2009. Influence of Andean uplift on climate and paleoaltimetry estimates. Earth and Planetary Science Letters 281(3-4), 238–248.

Eren, M., Kadir, S., Hatipoğlu, Z., Gül, M. 2008. Quaternary calcrete development in the Mersin area, southern Turkey. Turkish Journal of Earth Sciences 17(4), 763-784.

Farley, K. 2018. Helium diffusion parameters of hematite from a single-diffusion-domain crystal. Geochimica et Cosmochimica Acta 231, 117–129.

Foeken, J. P., Stuart, F. M., Dobson, K. J., Persano, C., Vilbert, D. 2006. A diode laser system for heating minerals for (U-Th)/He chronometry. Geochemistry, Geophysics, Geosystems 7(4), Q04015.

Hatzfeld, D., Molnar, P. 2010. Comparisons of the kinematics and deep structures of the Zagros and Himalaya and of the Iranian and Tibetan plateaus and geodynamic implications. Reviews of Geophysics 48(2), RG2005.

Heim, J. A., Vasconcelos, P. M., Shuster, D. L., Farley, K. A., Broadbent, G. 2006. Dating paleochannel iron ore by (U-Th)/He analysis of supergene goethite, Hamersley province, Australia, Geology 34(3), 173–176.

Henden, İ., Önder, E., Yurt, M. Z. 1978. Adana-Kayseri-Mansurlu - Karaköy - Attepe - Elmadağbeli-Kızılmevkii - Menteşdere - Uyuzpınarı demir madenleri Jeoloji ve Rezerv Raporu. MTA Derleme No: 6394 Ankara (unpublished).

Hofmann, F., Treffkorn, J., Farley, K. A. 2020. U-loss associated with laser-heating of hematite and goethite in vacuum during (U–Th)/He dating and prevention using high O_2 partial pressure. Chemical Geology 532, 119350.

Jaffey, N., Robertson, A. H. 2001. New sedientological and structural data from the Ecemiş Fault Zone, southern Turkey: implications for its timing and offset and the Cenozoic tectonic escape of Anatolia. Journal of the Geological Society 158(2), 367-378.

Jaffey, N., Robertson, A. 2005. Non-marine sedimentation associated with Oligocene-recent exhumation and uplift of the central Taurus mountains, S Turkey: Sedimentary Geology 173(1-4), 53–89.

Kaplan, M. Y., Eren, M., Kadir, S., Kapur, S. 2013. Mineralogical, geochemical and isotopic characteristics of Quaternary calcretes in the Adana region, southern Turkey: Implications on their origin. Catena 101, 164-177.

Kapur, S., Yaman, S., Gökçen, S. L., Yetiş, C. 1993. Soil stratigraphy and Quaternary caliche in the Misis area of the Adana Basin, southern Turkey. Catena 20(5), 431-445.

Kayseri-Özer, M. S. 2017. Cenozoic vegetation and climate change in Anatolia—a study based on the IPR-vegetation analysis. Palaeogeography, Palaeoclimatology, Palaeoecology 467, 37–68.

Ketcham, R. A. 2005. Forward and inverse modelling of low-temperature thermochronometry data. Reviews in Mineralogy and Geochemistry 58(1), 275–314.

Keskin, S. 2016. Attepe Demir Yatağı (Mansurlu Havzası, Adana) ve Çevresi Demir Yatakları ve Zuhurlarının Jeolojisi, Yapısal Özellikleri ve Tektoniği, PhD Thesis, Ankara Üniversitesi Fen Bilimleri Enstitüsü Doktora Tezi, 218 s., Ankara (unpublished).

Keskin, S., Ünlü, T. 2012. Geotectonic setting and structural controls of Elmadağbeli, Menteş, Karaçat, Kartalkaya and Attepe iron deposits (Kayseri-Adana Region, Türkiye). IESCA (International Earth Science Colloquium on the Aegean Region), IESCA-2012, Abstracts, 150.pp., İzmir.

Keskin, S., Ünlü, T. 2021. Tectonic Setting and Structural Controls of the Attepe Iron Deposits of Eastern Taurides, Türkiye. IOCENS-21. International Online Conferences On Engineering And Natural Sciences Oral Presentation in English. 5-7 September, Türkiye. Abstract Books page: 163.

Keskin, S., Ünlü, T. 2016*a*. Attepe Bölgesindeki Siderit Oluşumlarının Mineralojik Özellikleri ve Jeotektonik Ortamı (Kayseri-Adana Havzası, Türkiye). Hacettepe Üniversitesi, Yerbilimleri Dergisi 37 (2), 93-120.

Keskin, S., Ünlü, T. 2016*b*. Stable Isotope Studies in the Iron Deposits Around Attepe and Vicinity (Kayseri-Adana Region, Türkiye)**.** 69th Turkish Geological Congress Abstracts, MTA Cultural Center, April 11-15, 2016, Pages 158-159, Ankara.

Keskin, S., Ünlü, T., 2016*c*. Oxygen and Carbon Isotope Geochemistry of Pre-Cambrian Age Iron Deposits in the Attepe Area (Kayseri-Adana Basin, Türkiye)**.** VII International Geochemistry Symposium, Pages 89-90, May 16-18, 2016, Antalya, Türkiye.

Keskin, S., Ünlü, T., Coşkun, E. 2010. Geothermometric Studies in the Iron Deposits of Elmadağbeli, Menteş, Kartalkaya, and Mağarabeli (Kayseri-Adana Basin, Türkiye)**.** IV National Geochemistry Symposium, May 26-28, 2010, Page 137, Elazığ.

Küpeli, Ş. 2010. Trace and rare-earth element behaviors during alteration and mineralization in the Attepe iron deposits (Feke-Adana, southern Turkey), Journal of Geochemical Exploration 105(3), 51–74.

Küpeli, Ş., Karadağ, M. M., Ayhan, A., Döyen, A., Arık, F. 2007. C, O, S and Sr isotope studies on the genesis of Fe-carbonate and barite mineralizations in the Attepe iron district (Adana, southern Turkey), Geochemistry 67(4), 313–322.

Lee, M. R., Lindgren, P., Sofe, M. R. 2014. Aragonite, breunnerite, calcite and dolomite in the CM carbonaceous chondrites: High fidelity recorders of progressive parent body aqueous alteration. Geochimica et Cosmochimica Acta 144, 126-156.

Lisiecki, L. E., Raymo, M. E. 2005. A Pliocene-Pleistocene stack of 57 globally distributed benthic δ18O records. Paleoceanography 20 (1).

Litt, T., Pickarski, N., Heumann, G., Stockhecke, M., Tzedakis, P.C. 2014. A 600,000 year long continental pollen record from Lake Van, eastern Anatolia (Turkey). Quaternary Science Reviews 104, pp.30-41.

Lüdecke, T., Mikes, T., Rojay, F. B., Cosca, M. A., Mulch, A. 2013. Stable isotope-based reconstruction of Oligo-Miocene paleoenvironment and paleohydrology of central Anatolian lake basins (Turkey). Turkish Journal of Earth Sciences 22(5), 793–819.

Meesters, A., Dunai, T. 2005. A noniterative solution of the (U-Th)/He age equation. Geochemistry, Geophysics, Geosystems 6(4).

Meijers, M. J., Brocard, G. Y., Cosca, M. A., Lüdecke, T., Teyssier, C., Whitney, D. L., Mulch, A. 2018. Rapid late Miocene surface uplift of the central Anatolian plateau margin. Earth and Planetary Science Letters 497, 29–41.

Meijers, M. J., Brocard, G. Y., Whitney, D. L., Mulch, A. 2020. Paleoenvironmental conditions and drainage evolution of the Central Anatolian lake system (Turkey) during late Miocene to Pliocene surface uplift. Geosphere 16(2), 490–509.

Meijers, M. J., Strauss, B. E., Özkaptan, M., Feinberg, J. M., Mulch, A., Whitney, D. L., Kaymakçı, N. 2016. Age and paleoenvironmental reconstruction of partially remagnetized lacustrine sedimentary rocks (Oligocene Aktoprak basin, central Anatolia, Turkey), Geochemistry, Geophysics, Geosystems 17(3), 914–939.

Molnar, P. 2005. Mio-Pliocene growth of the Tibetan plateau and evolution of east Asian climate. Palaeontologia Electronica 8(1), 1–23.

Molnar, P., England, P., Martinod, J. 1993. Mantle dynamics, uplift of the Tibetan plateau, and the Indian monsoon. Reviews of Geophysics 31(4), 357–396.

Monshi, A., Foroughi, M. R., Monshi, M. R. 2012. Modified Scherrer equation to estimate more accurately nano-crystallite size using XRD. World Journal of Nano Science and Engineering 2(3), 154-160.

Moshi, H. P. 2014. Opportunities and challenges for the extraction of natural gas in Tanzania: The imperative of adequate preparedness. African Journal of Economic Review 2(1), 25–37.

Monteiro, H. S., Vasconcelos, P. M., Farley, K. A., Spier, C. A., Mello, C. L. 2014. (U–Th)/He geochronology of goethite and the origin and evolution of Cangas Geochimica et Cosmochimica Acta 131, 267–289.

Monteiro, H. S., Asconcelos, P. M., Farley, K., Lopes, C. A. M. 2018. Age and evolution of diachronous erosion surfaces in the Amazon; Combining (U-Th)/He and cosmogenic 3 He records. Geochimica et Cosmochimica Acta 229, 162–183.

Ocakoğlu, F. 2002. Palaeoenvironmental analysis of a Miocene basin in the high Taurus mountains (southern Turkey) and its palaeogeographical and structural significance. Geological Magazine 139(4), 473–487.

Öğretmen, N., Cipollari, P., Frezza, V., Faranda, C., Karanika, K., Gliozzi, E., Radeff, G., Cosentino, D. 2018. Evidence for 1.5 km of uplift of the Central Anatolian plateau's southern margin in the last 450 kyr and implications for its multiphased uplift history. Tectonics 37(1), 359–390.

Parlak, O., Karaoğlan, F., Rızaoğlu, T., Klötzli, U., Koller, F., Billor, Z. 2013. U–Pb and ^{40}Ar–^{39}Ar geochronology of the ophiolites and granitoids from the Tauride belt: Implications for the evolution of the inner Tauride suture. Journal of Geodynamics 65, 22–39.

Racano, S., Jara-Muñoz, J., Cosentino, D., Melnick, D. 2020. Variable quaternary uplift along the southern margin of the Central Anatolian plateau inferred from modelling marine terrace sequences. Tectonics 39, e2019TC005921.

Radeff, G. 2014. Geohistory of the Central Anatolian plateau southern margin (southern Turkey). PhD thesis, Potsdam University.

Robertson A.H.F., Dixon, J.E., 1984. Introduction: aspects of the geological evolution of the Eastern Mediterranean. Geological Society, London, Special Publications 17, 1-74.

Robertson, A. 2007. Overview of tectonic settings related to the rifting and opening of Mesozoicocean basins in the Eastern Tethys: Oman, Himalayas and Eastern Mediterranean regions. Geological Society, London, Special Publications Book Chapter.

Robertson, A., Grasso, M. 1995. Overview of the late Tertiary–recent tectonic and palaeo environmental development of the Mediterranean region. Terra Nova 7(2), 114–127.

Sarıkaya, M.A., Yıldırım, C., Çiner, A. 2015. Late Quaternary alluvial fans of Emli Valley in the Ecemiş Fault Zone, south central Turkey: Insights from cosmogenic nuclides. Geomorphology 228, pp.512-525.

Schemmel, F., Mikes, T., Rojay, B., Mulch, A. 2013. The impact of topography on isotopes in precipitation across the Central Anatolian plateau (Turkey), American Journal of Science 313(2), 61–80.

Schildgen, T.F., Cosentino, D., Bookhagen, B., Niedermann, S., Yıldırım, C., Echtler, H., Wittmann, H., Strecker, M. R. 2012. Multi-phased uplift of the southern margin of the Central Anatolian plateau, Turkey: A record of tectonic and upper mantle processes. Earth and Planetary Science Letters 317, 85–95.

Schildgen, T. F., Yıldırım, C., Cosentino, D., Strecker, M. R. 2014. Linking slab break-off, Hellenic trench retreat, and uplift of the Central and Eastern Anatolian plateaus. Earth Science Reviews 128, 147–168.

Speakman, R.J., Shanckley, M. S. 2013. Silo science and portable XRF in archaeology: a response to Frahm. Journal of Archaeological Science 40(2), 1435-1443.

Şengör, A. M. C., Yılmaz, Y. 1981. Tethyan evolution of Turkey: A plate tectonic approach. Tectonophysics 75, 181-241.

Şengör, A. M. C., Görür, N., Şaroğlu, F. 1985. Strike-slip faulting and related basin formation in zones of tectonic escape: Turkey as a case study. In: Biddle KT, Christie-Blick N (Eds.), Strikeslip Faulting and Basin Formation, Society of Economic Paleontologists and Mineralogists Special Publication 37, 227-264.

Şensoy, S. 2004. The mountains influence on Turkey Climate. In: Balwois Conference on Water Observation and Information System for Decision Support, Ministry of Environment and Physical Planning, p. 50-51.

Shuster, D. L., Vasconcelos, P. M., Heim, J. A., Farley, K. A. 2005 Weathering geochronology by (U-Th)/He dating of goethite. Geochimica et Cosmochimica Acta 514 69(3), 659–673.

Svenning, J. C. 2003. Deterministic Plio-Pleistocene extinctions in the European cool-temperate tree flora. Ecology Letters 6(7), 646-653.

Tardy, Y., Nahon, D. 1985. Geochemistry of laterites, stability of Al-goethite, Al-hematite, and Fe^{3+}-kaolinite in bauxites and ferricretes: an approach to the mechanism of concretion formation. American Journal of Science 285(10), 865-903.

Taylor, R. 2011. Boxworks and related features, in Gossans and Leached Cappings. Springer, 77–106.

Tiringa, D. 2016. Karaçat Demir Yatağı (Mansurlu Havzası, Adana) ve Doğusunda Yer Alan Demir Yatakları ve Zuhurlarının Jeolojisi. Ankara Üniversitesi Fen Bilimleri Enstitüsü Doktora Tezi, 283 s., Ankara (unpublished).

Tzedakis, P.C., Hooghiemstra, H., Pälike, H. 2006. The last 1.35 million years at Tenaghi Philippon: revised chronostratigraphy and long-term vegetation trends. Quaternary Science Reviews 25, 416-3430.

Vasconcelos, P.-M. 1999. K-Ar and $^{40}Ar/^{39}Ar$ geochronology of weathering processes. Annual Review of Earth and Planetary Sciences 27(1), 183–229.

Vasconcelos, P.-M., Heim, J. A., Farley, K. A., Monteiro, H., Waltenberg, K. 2013. $^{40}Ar/^{39}Ar$ and (U–Th)/He–$^{4}He/^{3}He$ geochronology of landscape evolution and channel iron deposit genesis at Lynn Peak, Western Australia, Geochimica et Cosmochimica Acta 117, 283–312.

Vasconcelos, P.-M., Reich, M., Shuster, D. L. 2015. The paleoclimatic signatures of supergene metal deposits. Elements 11(5), 317–322.

Wu, L.-Y., Stuart, F. M., Di Nicola, L., Heizler, M., Benvenuti, M., Hu, R.-Z. 2019. Multi-aliquot method for determining (U+ Th)/He ages of hydrothermal hematite: Returning to Elba. Chemical Geology 504, 151–157.

Yıldırım, C., Sarıkaya, M. A., Çiner, A. 2016. Late Pleistocene intraplate extension of the central Anatolian plateau, Turkey: Inferences from cosmogenic exposure dating of alluvial fan, landslide, and moraine surfaces along the Ecemiş fault zone. Tectonics 35(6), 1446– 1464.

Zachos, J., Pagani, M., Sloan, L., Thomas, E., Billups, K. 2001. Trends, rhythms, and aberrations in global climate 65 Ma to present. Science 292(5517), 686–693.